catalysts

MDPI

Article

Co-precipitation Synthesized MnO_x-CeO_2 Mixed Oxides for NO Oxidation and Enhanced Resistance to Low Concentration of SO_2 by Metal Addition

Jiaming Shao [1], Fawei Lin [2,*], Yan Li [3], Hairong Tang [1], Zhihua Wang [1,*], Peixi Liu [1] and Guanyi Chen [2]

1 State Key Laboratory of Clean Energy Utilization, Zhejiang University, Hangzhou 310027, China; shaojiaming@zju.edu.cn (J.S.); tanghair@zju.edu.cn (H.T.); liupx@zju.edu.cn (P.L.)
2 School of Environmental Science and Engineering, Tianjin University, Tianjin 300072, China; chen@tju.edu.cn
3 Shenhua Guohua (Beijing) Electric Power Research Institute Co., Ltd., Beijing 100025, China; heiheiyaner@zju.edu.cn
* Correspondence: linfawei@tju.edu.cn (F.L.); wangzh@zju.edu.cn (Z.W.); Tel.: +86-022-87402075 (F.L.); +86-0571-87953162 (Z.W.); Fax: +86-022-87402075 (F.L.); +86-0571-87951616 (Z.W.)

Received: 18 May 2019; Accepted: 6 June 2019; Published: 12 June 2019

Abstract: NO oxidation was conducted over MnO_x-CeO_2 catalysts, which were synthesized by the co-precipitation method. The calcination temperature and third metal doping were the main considerations. MnCe catalysts calcined at 350 °C and 450 °C attained the highest NO conversion efficiency, compared to 550 °C. XRD results suggested that the higher the calcination temperature, the higher the crystallization degree, which led to a negative effect on catalytic activity. Subsequently, Sn, Fe, Co, Cr, and Cu were separately doped into MnCe composites, but no improvement was observed for these trimetallic catalysts in NO conversion. Nevertheless, MnCeSn, MnCeFe, and MnCeCo still exhibited a desirable NO conversion efficiency, so they were tested under SO_2 addition together with MnCe catalyst. Among them, MnCeFe exhibited the highest NO conversion after whole poisoning testing. XPS results indicated that Fe could protect Mn and Ce metal oxides from being reduced during SO_2 poisoning process. Furthermore, in in-situ DRIFTS measurement, part of nitrate species maintained undestroyed on the MnCeFe catalyst surface after SO_2 poisoning. These characteristics reinforced that Fe dropping would achieve better performance under SO_2 atmosphere.

Keywords: MnO_x-CeO_2; co-precipitation; NO oxidation; SO_2 resistance; metal addition

1. Introduction

BP's Energy Outlook (2016) predicted that fossil fuels would still maintain the dominant sources of the world energy powering until 2035 [1]. Power plants, industrial boilers, and motor vehicle engine discharge NO_x via fossil fuels combustion inevitably [2]. After complex atmospheric chemical reactions, exhausted NO_x will be converted to the culprit of many typical environmental events, such as photochemical smog, ozone depletion, acid rain, and green-house effect [3–5]. Conventionally, the three-layer SCR (selective catalytic reduction) catalyst, assembled in coal-fired power plants, could satisfy the ultra-low emission standard in China (i.e., NO_x < 50 mg·Nm^{-3}) [6]. However, the short slab of strict temperature window impedes the SCR application in industrial boilers, which produce steel, ceramic, glass, and cement, with relatively low temperature flue gas (i.e., <200 °C). Typically, 95% of NO_x in the exhaust gas is water-insoluble NO, but it can be easily be removed by wet scrubbing after oxidation to NO_2 [7,8]. Therefore, NO oxidation technology is considered an

alternative for NO_x elimination, and it is also a critical step in SCR, LNT (lean NO_x trap), and NSR (NO_x storage-reduction) [9–11].

Transition metal oxides (TMO) are excellent candidates, given their rich various oxidation states, abundant oxygen defects, and earth rich features [12–14]. Among these catalysts, Mn-based, Ce-based, and Zr-based catalysts exhibit excellent performance at low temperature, and their SO_2 resistance was enhanced after the modification of other TMO [4,15–17]. In particular, the strong interaction between Mn and Ce created remarkable oxygen storage and redox ability [15,18], which contributed to extensive application in NO [19], as well as soot [20,21], mercury [22,23], VOCs [24,25] oxidation reactions. Lin et al. [26] synthesized Mn/CeO_x catalyst by the sol-gel method and reported ~90% NO conversion at 230 °C under the GHSV (Gas Hour Space Velocity) of 20,000 h^{-1}. Liu et al. [27] demonstrated that plasma assisted synthesis of Mn-Ce-O_x catalyst produced abundant Ce^{3+} species and active oxygen species, leading to better catalytic behavior. To further lower the efficient catalytic temperature, Shen et al. [28] employed carbon as a hard template to prepare a series of hollow MnO_x-CeO_2. Among them, the sample equipped with the largest surface area and pore volume values exhibited the best performance, whereby the maximum NO oxidation conversion (~82%) was obtained at 200 °C with 120,000 h^{-1} GHSV. Recently, trimetallic catalysts, Mn-Co-Ce-O_x [1,15], Mn-Ce-Zr-O_x [19], Cu-Ce-Zr-O_x [29], attracted much attention in relation to mitigating SO_2 poisoning. However, the catalyst stability under SO_2 is still a hard nut to crack.

Considering industrial production, co-precipitation method has unique advantages in cost and process simplification compared with aforesaid sol-gel, plasma and template methods. In this paper, MnO_x-CeO_2 composites catalysts were synthesized by ammonium carbonate co-precipitation method. Sn, Fe, Co, Cr, Cu, the most commonly used TMO, were introduced to investigate their effect on activity and SO_2 resistance. Unfortunately, the oxidation atmosphere might have a positive effect on sulfuration [30], while no efficient method to avoid SO_2 poisoning exists. A shift in attention to low-sulfur flue gas is a better way to understand the SO_2 poisoning process in detail. In addition, the catalyst resistance under low concentration SO_2 has been rarely researched, which might have a broad application space in low-sulfur fuel combustion. Therefore, the investigation of low SO_2 resistance was carried out in this paper. XRD, XPS, BET and H_2-TPR were used to investigate the catalyst activity, and in-situ DRIFTS measurements were conducted to reveal the NO oxidation and SO_2 poisoning process.

2. Results and Discussion

2.1. XRD and BET Results

The XRD patterns of MnO_x-CeO_2 based catalysts, with different calcination temperatures and metal doping, are shown in Figure 1. All these catalysts consisted of diffraction peaks that corresponded to CeO_2 with a cubic fluorite structure. These diffraction peaks at 28.6°, 33.1°, 47.5°, 56.3°, 59.1°, 69.4°, 76.7°, 79.1°, and 88.4° are assigned to the crystalline planes of CeO_2 (111), (200), (220), (311), (222), (400), (331), (420), and (422) (JCPDS:34-0394) [31]. No diffraction peaks that correlated with MnO_x species were detected, indicating metals doping did not destroy the framework of CeO_2 [30,32,33]. The ionic radius of Mn^{3+} is 0.066, and Ce^{4+} is 0.1098 nm. Therefore, Mn^{3+} might incorporate into the fluorite lattice of CeO_2. Machida et al. [34] also found that Mn_2O_3 crystallization could be detected until Mn/(Mn+Ce) > 0.75, whereas it was 0.29 in this paper.

The diffraction peaks intensified with the increased calcination temperature, as shown in Figure 1a, which was consistent with the increasing crystallite size determined by Scherrer equation for (111) peak in Table 1. Clearly, increasing calcination temperature gave rise to a higher degree of crystallization, and resulted in lower catalytic activity. Figure 1b presents XRD patterns of MnO_x-CeO_2 with third metal doping. Obviously, no new diffraction peaks appeared after metal doping. The peaks of CeO_2 became broader and the intensity weakened significantly, especially for MnCeSn and MnCeCr. Also, their crystallite sizes reduced to 8.8 nm, and 9.9 nm, respectively (Table 1).

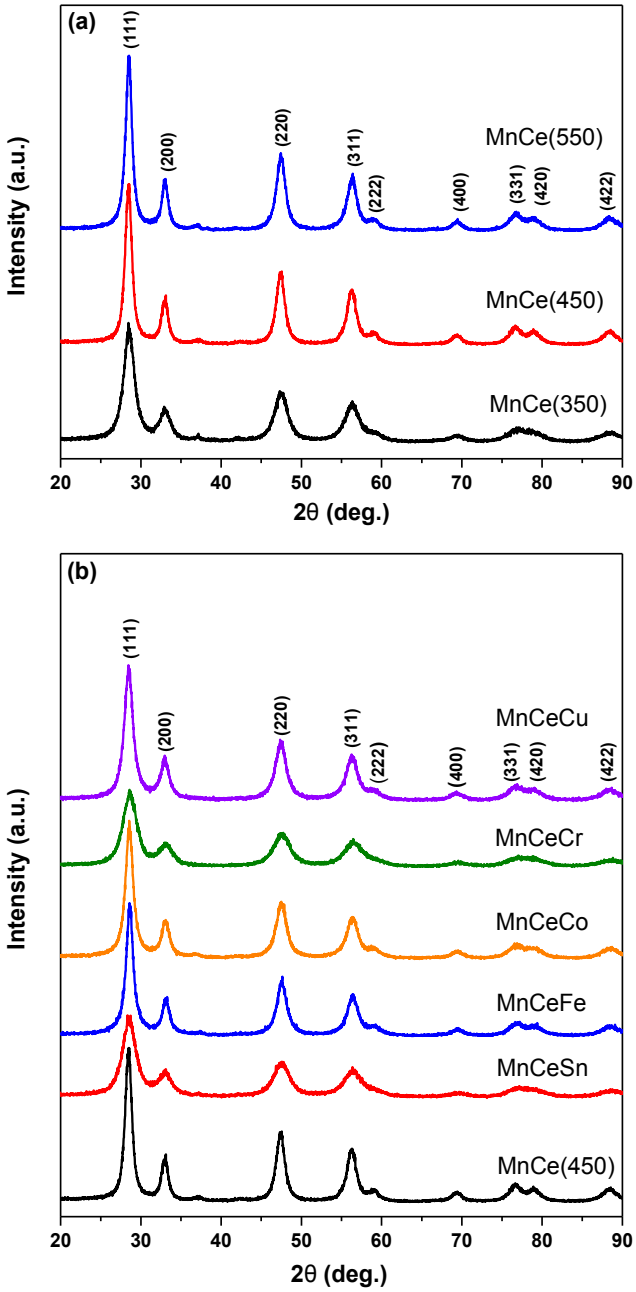

Figure 1. XRD patterns of MnO_x-CeO_2 based catalysts, (**a**) MnO_x-CeO_2 with different calcination temperature, (**b**) MnO_x-CeO_2 with metal doping.

Table 1. Crystallization properties of MnO_x-CeO_2 based catalysts.

Catalyst	$2\theta_{(111)}$/°	FWHM	Crystallite Size [a]/nm
MnCe(350)	28.6	0.902	9.9
MnCe(450)	28.4	0.729	11.6
MnCe(550)	28.5	0.737	12.1
MnCeSn	28.6	1.017	8.8
MnCeFe	28.6	0.742	12.1
MnCeCo	28.6	0.772	11.6
MnCeCr	28.7	0.901	9.9
MnCeCu	28.5	0.792	11.3

[a] Crystalline size determined from Scherrer equation for (111) peak.

The textural properties of MnO_x-CeO_2 based catalysts are summarized in Table 2. Clearly, the surface area and pore volume of the trimetallic catalysts (MnCeSn, MnCeFe, and MnCeCr) were higher than that of the bimetallic catalyst (MnCe(450)). MnCeCo exhibited higher surface area, but lower pore volume compared with MnCe(450). However, the surface area and pore volume of MnCeCu were all smaller than MnCe(450). Among them, MnCeSn and MnCeCr possessed distinct increase in both surface area and pore volume, i.e., 106.6 $m^2 \cdot g^{-1}$ and 0.19 $mL \cdot g^{-1}$ for MnCeSn, 126.5 $m^2 \cdot g^{-1}$ and 0.26 $mL \cdot g^{-1}$ for MnCeCr. This was consistent with the obvious broader and weaker diffraction peaks of MnCeSn and MnCeCr in XRD patterns. Lower crystallization degree implied better pore structure, i.e., high surface area and pore volume. Generally, higher surface area and pore volume can provide more active adsorption sites for reactants, but these trimetallic catalysts didn't exhibit fortunately higher activity. Especially, MnCeCr possessed the lowest NO oxidation activity in the activity test, even with the highest surface area and pore volume, indicating that the surface area is not the only factor for catalytic activity. This observation may be explained by their reducibility from TPR results next.

Table 2. Textural properties of MnO_x-CeO_2 based catalysts.

Catalyst	BET Surface Area/$m^2 \cdot g^{-1}$	Pore Volume [a]/$mL \cdot g^{-1}$	Avg. Pore Diameter [b]/nm
MnCe(450)	73.3	0.10	9.8
MnCeSn	106.6	0.19	14.1
MnCeFe	111.7	0.11	5.5
MnCeCo	95.9	0.08	5.0
MnCeCr	126.5	0.26	14.3
MnCeCu	63.8	0.07	7.7

[a] Single point adsorption total pore volume of pores less than 40.3 nm diameter at $P/P_0 = 0.95$. [b] BJH desorption average pore diameter.

2.2. H_2-TPR Measurements

The H_2-TPR profiles of trimetallic catalysts are shown in Figure 2, and MnCe(450) was listed as a benchmark. Except for MnCeCu, there were two dominant reduction peaks for these catalysts, which were mainly assigned to MnO_x species three-step reduction: $MnO_2 \rightarrow Mn_2O_3 \rightarrow Mn_3O_4 \rightarrow MnO$ [35,36]. Additionally, a weak tail peak, at a temperature higher than 400 °C, should be attributed to the reduction of the bulk Ce^{4+} to Ce^{3+} [37,38]. Obviously, the third metal was reduced at the similar reduction temperature range of MnO_x species. On the other hand, the third metal doping resulted in distorted H_2 reduction profiles, which led to the reduction profiles shifting to a higher temperature. These observations should be attributed to the metal interaction. Reducibility is a critical factor for NO oxidation. As the NO conversion curves of the activity test, the highest points were located near 250 °C. Therefore, the H_2 reduction profiles at temperature lower than or nearby to 250 °C are mainly correlated with the NO oxidation activity. Compared to MnCe(450), the first reduction peak at ~265 °C of the trimetallic catalysts was weaker, but the second peak at 330~400 °C intensified. As to MnCeCr, the two reduction peaks incorporated together, and the reduction temperature shifted to higher level entirely. These changes in reducibility after the third metal addition gave an explanation for their worse catalytic activity, even with better pore structure parameters (Table 2). The first H_2 reduction peak of MnCeSn, MnCeFe, and MnCeCo did not shift to a higher temperature, which was correlated with their relatively better activities. Due to the intrinsic, significantly low temperature reducibility of Cu, its doping resulted in the original MnO_x species reduction peaks moving to a lower temperature (<250 °C). The synergistic effect between CuO_x and MnO_x species contributed to more oxygen defects and structural distortion, then enhanced low temperature reducibility [39]. Nevertheless, the catalytic activity of MnCeCu still became worse compared with MnCe(450) in the activity test. As mentioned in Table 2, the surface area and pore volume of MnCeCu were the lowest among all the catalysts, which was unfavorable for reactants adsorption. On the other hand, a strong reducibility of Cu caused the reduction of Mn species [40]. NO oxidation proceeded through the MnO_x species valance state

transformation between Mn^{4+} and Mn^{3+} [30,41]. Therefore, Mn ions reduction by Cu would inhibit NO oxidation reaction, and gave rise to the low catalytic activity of MnCeCu.

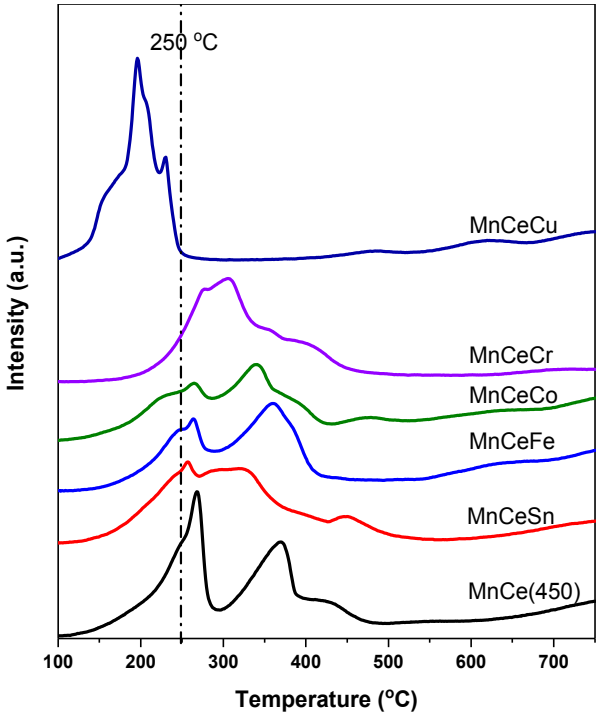

Figure 2. H_2-TPR profiles of MnCe(450), MnCeSn, MnCeFe, MnCeCo, MnCeCr, and MnCeCu.

2.3. XPS Analysis

XPS characterization of MnCe(450) (abbreviated as MnCe) and MnCeFe was conducted to investigate the oxidation state of Mn, Ce, and the distribution of O species. The XP spectra of Mn 2p included two regions, i.e., Mn $2p_{3/2}$ and Mn $2p_{1/2}$. The region of Mn $2p_{3/2}$ was deconvoluted into two peaks using Gaussian functions, as presented in Figure 3a. These two peaks were assigned to Mn^{3+} and Mn^{4+} [36,42] from low, to high binding energies, respectively. The binding energies and respective ratios estimated by integration are tabulated in Table 3. Notably, the binding energies shifted to higher value after Fe doping caused by electron transfer. The decrease in Mn^{4+} ratios demonstrates Mn ions reduction caused by Fe doping, which should be related to the lower activity in NO oxidation.

The Ce 3d spectra shown in Figure 3b exhibited complicated overlapping peaks and were deconvoluted into eight peaks after peak-fit processing. These peaks were assigned to two regions, i.e., Ce $3d_{3/2}$ and Ce $3d_{5/2}$, and the corresponding peaks were labelled as U and V series. The detailed binding energies and Ce^{4+} ratios are tabulated in Table 4. Two satellite peaks of U′ and V′ were assigned to Ce^{3+}, and the other peaks were characteristic of Ce^{4+} [31,43]. The relative Ce^{4+} content in the catalyst was proportional to the crystallite size [44], and it was also supported by the XRD patterns. Ce^{3+} ions represent reduced, non-stoichiometric cerium species. The co-existence of Ce^{4+} and Ce^{3+}, as well as Mn^{4+} and Mn^{3+}, provided electron exchange for the redox reactions, and then contributed to the catalytic activity in NO oxidation. Notably, the ratio of Ce^{4+}/Ce increased from 56.2% (MnCe) to 65.9% (MnCeFe) after Fe doping. Overall, Ce^{3+} was oxidized into higher oxidation state, and Mn^{4+} was reduced into lower oxidation state after Fe doping into MnCe mixed oxides.

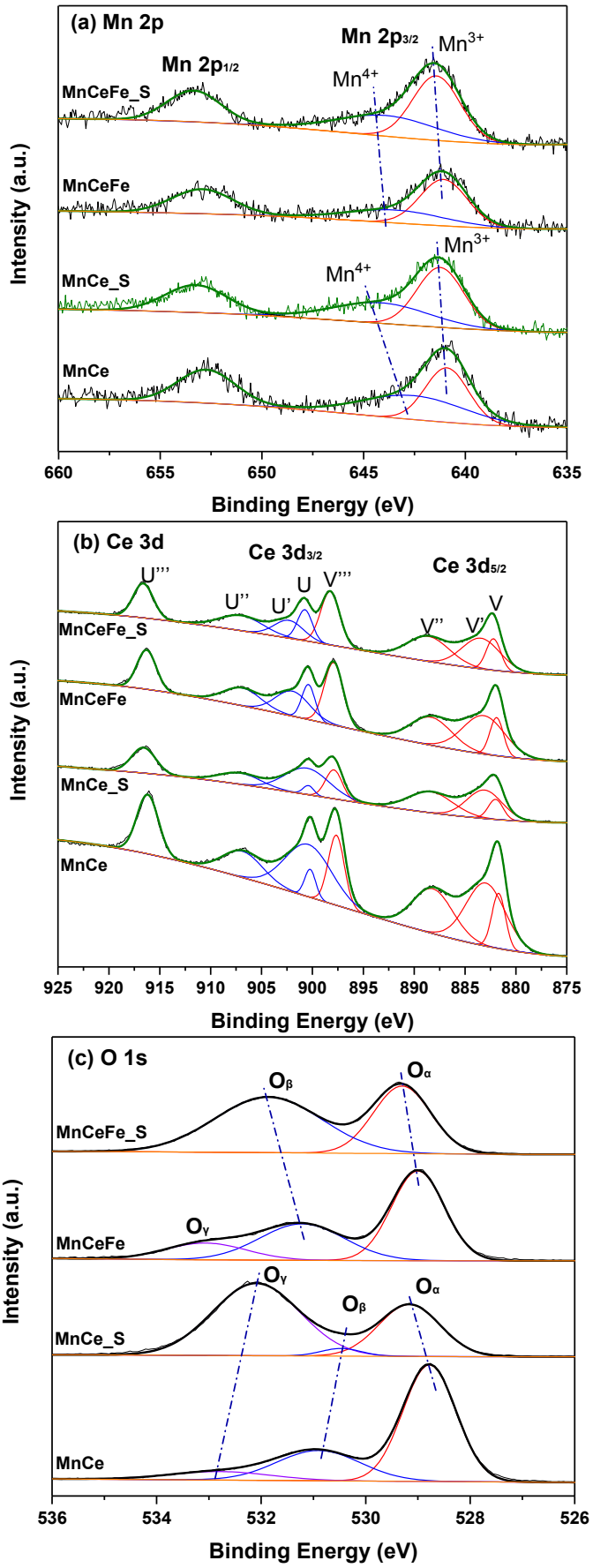

Figure 3. XP spectra of MnCe, MnCe_S, MnCeFe, and MnCeFe_S, (**a**) Mn 2p, (**b**) Ce 3d, (**c**) O 1s.

Table 3. 2p XPS parameters of MnCe, MnCe_S, MnCeFe, and MnCeFe_S.

Catalyst	Mn^{3+}		Mn^{4+}	
	B.E. (eV)	Mn^{3+}/Mn^{n+} (%)	B.E. (eV)	Mn^{4+}/Mn^{n+} (%)
MnCe	640.9	48.9	642.5	51.1
MnCe_S	641.2	58.5	644.1	41.5
MnCeFe	641.1	63.5	643.4	36.5
MnCeFe_S	641.4	60.1	643.9	39.9

Table 4. Ce 3d XPS parameters of MnCe, MnCe_S, MnCeFe and MnCeFe_S.

Catalyst	Ce^{4+}						Ce^{3+}		Ce^{4+}/Ce
	V	V″	V‴	U	U″	U‴	V′	U′	%
MnCe	881.7	888.2	897.7	900.2	906.9	916.2	883.0	900.4	56.2
MnCe_S	882.0	888.4	897.9	900.4	907.2	916.6	883.1	900.5	57.2
MnCeFe	881.9	888.3	897.9	900.4	906.9	916.3	883.2	902.0	65.9
MnCeFe_S	882.2	888.6	898.2	900.7	907.0	916.6	883.4	902.3	72.1

The O 1s XP spectra are presented in Figure 3c that are classified into two main bands. After the deconvolution process, two or three characteristic peaks were observed, with the corresponding binding energies tabulated in Table 5. From low to high binding energies, these peaks were assigned to O_α, O_β, and O_γ, respectively. O_α represents lattice oxygen, while the surface adsorbed oxygen, hydroxyl groups and carbonates are associated with O_β, and O_γ [31], respectively. The distribution ratios of oxygen species are listed in Table 5. Clearly, the ratio of O_β and O_γ increased from 26.3% and 8.9% (MnCe) to 33.6% and 14.8% (MnCeFe), demonstrating more surface oxygen species was created after Fe addition.

Table 5. O 1s XPS parameters of MnCe, MnCe_S, MnCeFe, and MnCeFe_S.

Catalyst	O_α		O_β		O_γ	
	B.E. (eV)	O_α/O (%)	B.E. (eV)	O_β/O (%)	B.E. (eV)	O_γ/O (%)
MnCe	528.8	64.8	530.9	26.3	532.8	8.9
MnCe_S	529.2	32.6	530.5	3.1	532.1	64.3
MnCeFe	529.0	51.6	531.2	33.6	533.1	14.8
MnCeFe_S	529.3	39.4	531.9	60.6	–	–

2.4. Catalytic Activity

2.4.1. MnO_x-CeO_2 with Different Calcination Temperature

Carbonate composites of $Ce_2(CO_3)_3$ and $Mn(CO_3)_2$ were formed after the co-precipitation process via Equations (1) and (2). Composite oxides of MnO_x and CeO_2 were then produced via carbonate decomposition after the calcination process. To investigate the effect of calcination temperature on NO oxidation, three catalysts calcined at 350 °C, 450 °C, and 550 °C were prepared, and the corresponding catalytic activities are shown in Figure 4. The dot line is the thermodynamic limitation curve for NO oxidation. MnCe(350) and MnCe(450) exhibited similar NO conversion within the whole temperature range, whereas a distinct decrease in NO conversion was observed for MnCe(550). MnCe(350) and MnCe(450) achieved the highest NO conversion efficiency of ~88% at 220~250 °C. But, only 83% was obtained as the highest value for MnCe(550) at 280 °C. Therefore, the calcination temperature was a significant synthesis factor for NO oxidation, and 350~450 °C was a comparatively suitable range for MnCe catalyst calcination. Table 6 illustrated the NO oxidation activities of metal-oxides in literatures.

It can be seen that the MnCe catalyst in our paper has a relatively high NO conversion efficiency at low temperature:

$$2Ce(NO_3)_3 + 3(NH_4)_2CO_3 \rightarrow Ce_2(CO_3)_3 + 6NH_4NO_3. \quad (1)$$

$$Mn(CH_3COO)_2 + (NH_4)_2CO_3 \rightarrow MnCO_3 + 2CH_3COONH_4. \quad (2)$$

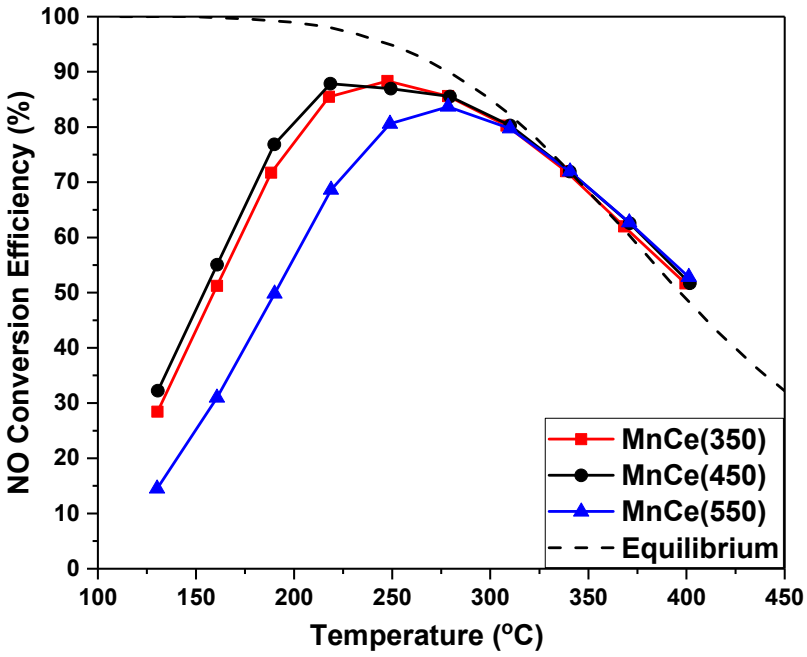

Figure 4. NO conversion over MnO_x-CeO_2 with different calcination temperature.

Table 6. Summary of the metal oxides catalytic activities in literatures.

Catalyst	Preparation Method	Reaction Condition	NO Conversion	Ref
MnCe	Co-precipitation	200 ppm NO, 10% O_2, 15,000 h^{-1}, 220 °C	88%	This paper
$MnCeO_x$	Citric acid method	500 ppm NO, 3% O_2, 50,902 h^{-1},150 °C	46%	[45]
$MnCeO_x$	Sol-gel method	400 ppm NO, 5% O_2, 360,000 h^{-1}, 300 °C	65%	[27]
$MnCeO_x$	Co-precipitation	200 ppm NO, 8% O_2, 5% H_2O, 8% CO_2, 25,000 h^{-1}, 350 °C	69%	[19]
$MnCeO_x$	CS template method	250 ppm NO, 5% O_2, 120,000 h^{-1}, 220 °C	82%	[28]
$CrCeO_x$	Hydro-thermal method	400 ppm NO, 8% O_2, 35,400 h^{-1}, 300 °C	66%	[46]
$CeCoO_x$	Sol-gel method	300 ppm NO, 10% O_2, 20,000 h^{-1}, 230 °C	93%	[26]
$SmMn_2O_5$	Co-precipitation	400 ppm NO, 10% O_2, 100,000 h^{-1}, 330 °C	52%	[47]
$Cu/Ce_{0.8}Zr_{0.2}O_2$	Deposition-precipitation	500 ppm NO, 5% O_2, 80,000 h^{-1}, 320 °C	73%	[29]
$MnCeCoO_x$	Co-precipitation	500 ppm NO, 3% O_2, 35000 h^{-1}, 150 °C	80%	[48]
$CoZrCeO_x$	Citrate complexation	3900 ppm NO, 8% O_2, 30,000 h^{-1}, 300 °C	80%	[49]

2.4.2. MnO_x-CeO_2 with Metal Doping

MnCe(450) was used as the benchmark catalyst, while Sn, Fe, Co, Cr, and Cu was added separately into MnO_x-CeO_2 composite oxides as the doping metal, and their catalytic activities are shown in Figure 5. Unfortunately, no improvement could be observed for all these doping catalysts, whereas different degrees of decrease are presented. Similar NO conversion curves were presented for MnCeSn, MnCeFe, and MnCeCo. They obtained the highest NO conversion efficiency of ~85%, but it was first observed until 250 °C. For MnCeCu and MnCeCr, the NO conversion curves further shifted to higher temperature. MnCeCr exhibited the worst catalytic activity, i.e., the highest value was 70% at 310 °C.

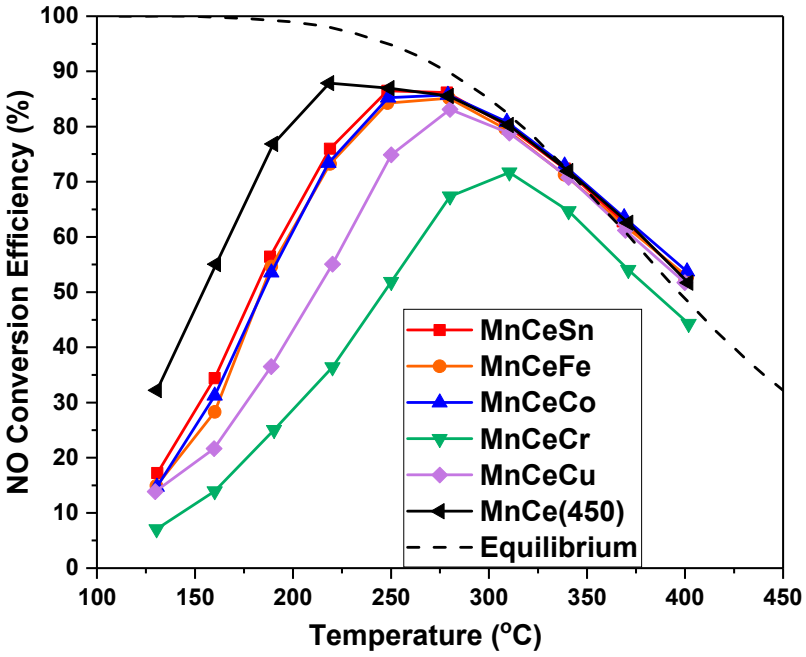

Figure 5. NO conversion over MnO_x-CeO_2 with metal doping.

2.5. Catalyst Resistance to SO_2

2.5.1. Variation of NO Oxidation with SO_2 Addition

To investigate the effect of SO_2 on catalytic activity in NO oxidation, low concentration of SO_2, i.e., 20 ppm, was introduced into a catalytic reactor to observe the slow poisoning process. SO_2 poisoning was investigated on MnCe, MnCeFe, MnCeSn, and MnCeCo catalyst. The NO conversion curves at 250 °C along with time on stream are presented in Figure 6. The 13 h testing can be divided into four sections, i.e., temperature ramp to 250 °C within 2 h, stabilization within 100 min, SO_2 addition with staged concentrations (20~40~20 ppm), and non-SO_2. The concentrations of NO and NO_2 in the entire process are also recorded for comparison. A similar tendency of NO and NO_2 concentration curves can be observed in the temperature ramp section in Figure 6a–d. Initially, NO concentration increased to a specific value. Next, NO concentration drastically decreased after a previous increase, which is likely related to the promoted adsorption at a certain temperature. The sharp decline was found between two peaks for NO concentration curves. Meanwhile, NO_2 appeared right on the heels of the NO concentration valley bottom. After saturation adsorption, just at the valley bottom position, further increased temperature caused desorption of NO and NO_2. When the temperature reached a starting value for NO oxidation, NO concentration decreased again, whilst NO_2 concentration further increased until stabilization.

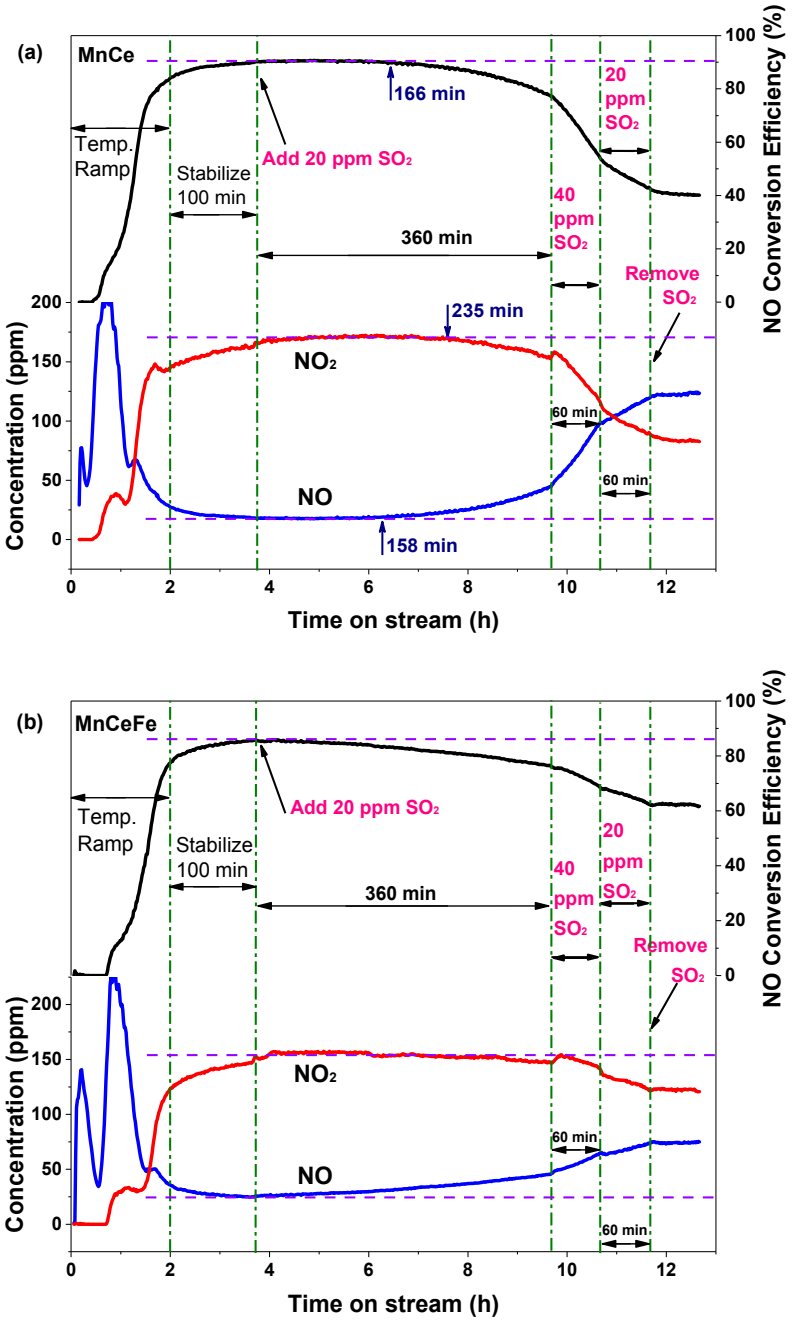

Figure 6. *Cont.*

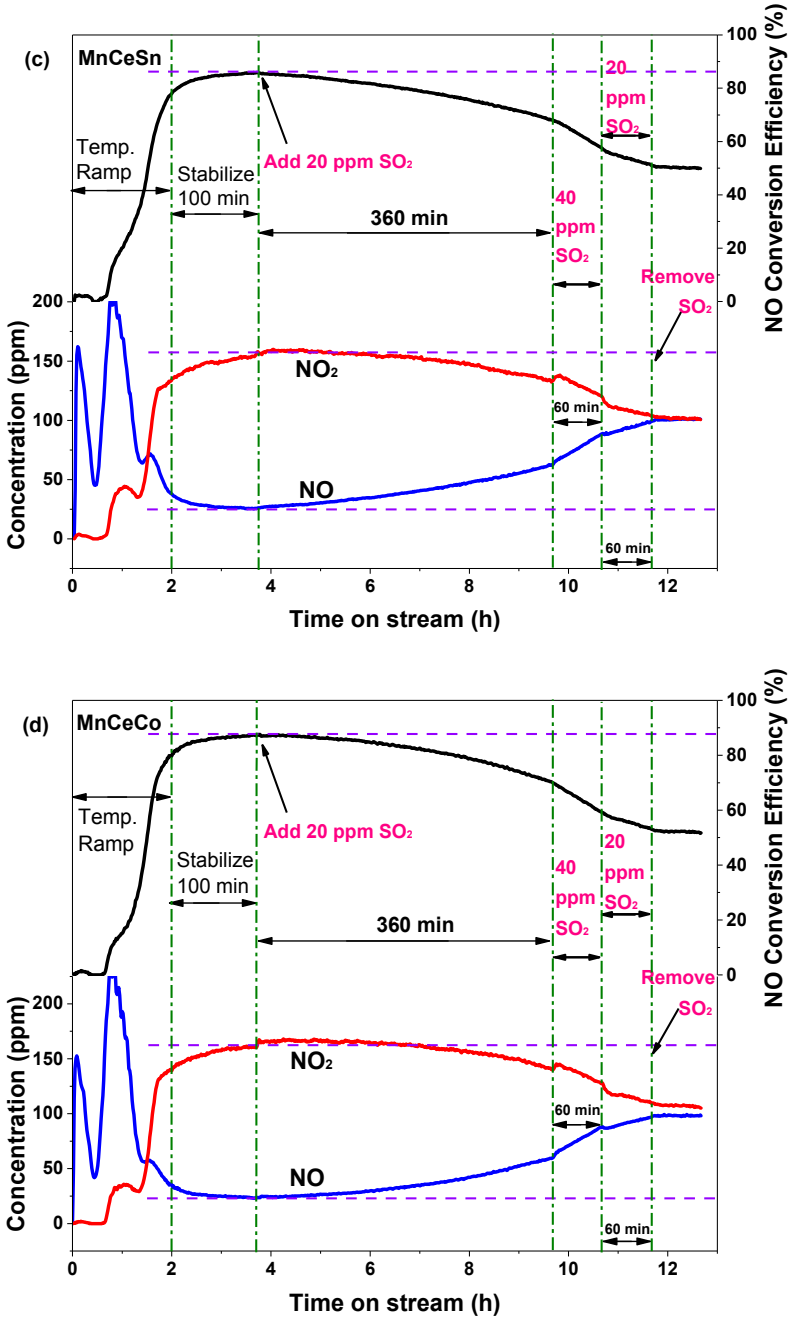

Figure 6. Effect of SO_2 on NO conversion efficiency at 250 °C: (**a**) MnCe, (**b**) MnCeFe, (**c**) MnCeSn, and (**d**) MnCeCo.

The detailed NO conversion efficiency values, at four critical points, are summarized in Table 7. After 100 min stabilization, NO conversion efficiencies of these catalysts all reached their highest values. When SO_2 was injected into the reactor, NO conversion of MnCe maintained the highest value for 166 min, and then decreased to 77% at the end of the first 360 min. However, unlike MnCe, the NO conversion efficiency of MnCeFe, MnCeSn, and MnCeCo decreased immediately once 20 ppm SO_2 addition, reaching to 76%, 68%, and 70% after 360 min test, respectively. Compared with the decrement from 86% to 76% of MnCeFe, the descending rate for MnCe seems to be relatively steeper from 90% to 77%. Interestingly, NO concentration always increased later than the decrease of NO_2 concentration. This phenomenon was ascribed to the NO_2 desorption expelled by sulfate formation on the catalyst surface, resulting in a relatively delayed NO_2 concentration. Almost no reduction in NO_2 concentration was observed for MnCeFe during 360-min SO_2 poisoning testing (20 ppm), indicating

excellent NO_2 storage capacity. Subsequently, SO_2 concentration was increased to 40 ppm. Clearly, the decline in NO conversion sped up, especially for MnCe, i.e., which reduced 23%, from 77% to 54% in 60 min. According to the data in Table 7, the total decrement within this 60-min poisoning process of MnCeFe, MnCeSn, and MnCeCo were 7%, 11%, and 12%, respectively. This indicates trimetallic catalysts improved the resistance to SO_2 with relatively higher concentration. When the SO_2 concentration was switched back to 20 ppm, the decline rate was alleviated except for MnCeFe. It is worth mentioning that the decrement of NO conversion efficiency for MnCe was unexpectedly the highest, although it was the latest one to start decreasing in the first 360-min poisoning. NO conversion efficiency remained stable when SO_2 was dislodged from simulated flue gas for all the four catalysts. Overall, MnCeFe exhibited the highest resistance to SO_2, which possessed 62% NO conversion efficiency after whole poisoning testing.

Table 7. NO conversion efficiency values at four critical points.

Catalyst	Highest Value	360-min (20 ppm SO_2)	60-min (40 ppm SO_2)	60-min (20 ppm SO_2)
MnCe	90%	77%	54%	42%
MnCeFe	86%	76%	69%	62%
MnCeSn	86%	68%	57%	51%
MnCeCo	87%	70%	58%	53%

2.5.2. Surface Properties after SO_2 Poisoning Process

The oxidation states of Mn, Ce, Fe, and the distribution of O species before, and after, the SO_2 poisoning process were investigated by XPS characterization. The XP spectra of Mn 2p, Ce 3d, and O 1s are presented in Figure 3, with the detailed binding energies and ratios tabulated in Tables 3–5. Clearly, the most distinct changes occurred in the O 1s spectra, i.e., the lattice oxygen (O_α) decreased and transformed into surface adsorbed oxygen species (O_β and O_γ) after SO_2 poisoning process. This observation should be mainly attributed to the accumulation of sulfate species on the catalyst surface [30]. Additionally, changes in Mn 2p and Ce 3d were different for MnCe and MnCeFe. The ratio of Mn^{4+} of MnCe decreased from 51.1% to 41.5% after the SO_2 poisoning process; whereas, it increased a little from 36.5% to 39.9% for MnCeFe. In terms of Ce 3d, these two catalysts all exhibited increase in Ce^{4+} ratio after SO_2 addition. Generally, the formation of sulfate species on catalyst surface would reduce the metal oxides oxidation state. For MnCe catalyst, reduction of metal oxidation state was mainly occurred in Mn ions. However, no reduction was found in both Mn ions and Ce ions for MnCeFe catalyst. It can be speculated that Fe ions took this responsibility instead of Mn. Therefore, Fe 2p XP spectra were carried out, shown in Figure 7, and it was deconvoluted into four peaks using Gaussian functions. These peaks were assigned to Fe^{3+}, Fe^{2+} and satellite peaks from low to high binding energy. The corresponding binding energies and ratios of Fe ions are tabulated in Table 8. Obviously, Fe^{3+} decreased from 41.2% to 21.9% accompanied by the increase of Fe^{2+}. Herein, Fe played a protective role in the reduction of Mn and Ce when SO_2 was added, and as a result, the SO_2 resistance was enhanced.

Table 8. Fe 2p XPS parameters of MnCeFe and MnCeFe_S.

Catalyst	Fe^{3+}		Fe^{2+}	
	B.E. (eV)	Fe^{3+}/Fe (%)	B.E. (eV)	Fe^{2+}/Fe (%)
MnCeFe	709.9	41.2	712.0	58.8
MnCeFe_S	710.1	21.9	711.1	78.1

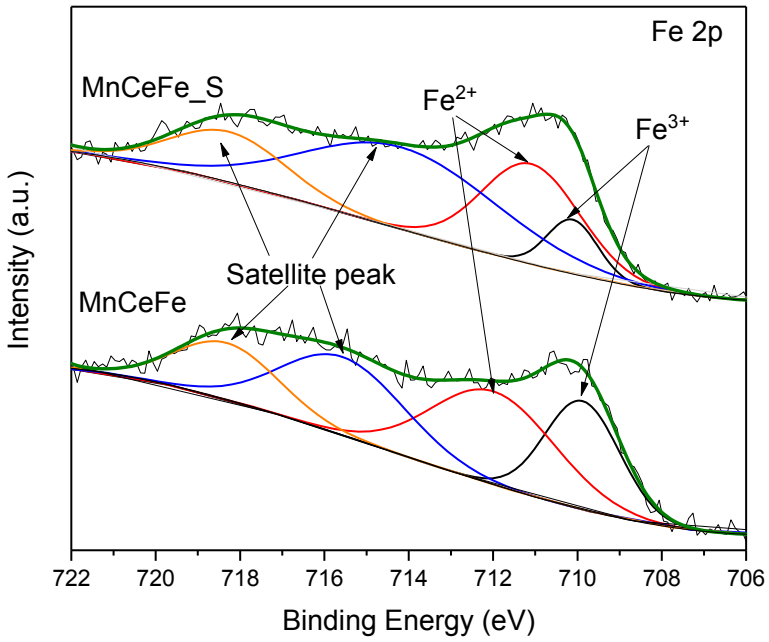

Figure 7. Fe 2p XP spectra of MnCeFe and MnCeFe_S.

2.5.3. In-Situ DRIFTS Measurement

In-situ DRIFTS measurements were conducted, in order to investigate the surface species formation during NO oxidation and the SO_2 poisoning process. The infrared absorption spectra of NO (200 ppm)-O_2 (10%) co-adsorption and NO-O_2-SO_2 co-adsorption at 250 °C were collected successively, as listed in Figures 8 and 9. Firstly, diverse absorption bands emerged after NO and O_2 injection, which were assigned to nitrate and nitrite species. For MnCe catalyst, shown in Figure 8a, the dominated bands at 1311 cm^{-1}, 1382 cm^{-1}, and 1473 cm^{-1} were associated to bridged nitrate [50,51], adsorbed NO_3^- [52], and cis-$N_2O_2^{2-}$ [32], respectively. Several weak bands (903 cm^{-1}, 832 cm^{-1}, and 813 cm^{-1}), lower than 1043 cm^{-1}, should be assigned to nitrate species on manganese and cerium oxides [32]. All the appeared peaks increased quickly at first 30 min, and then maintained at a certain level, indicating saturation adsorption. These nitrate and nitrite species on the catalyst surface were considered as the critical intermediates for NO oxidation. After 60-min co-adsorption of NO-O_2, SO_2 was added, and the infrared absorption spectra are presented in Figure 8b. In the first 40 min, only 20 ppm SO_2 was added. The band at 1114 cm^{-1} increased first, which corresponded to the bulk-like bidentate sulfate species [53–56], and developed into the dominated band finally. Subsequently, the bands at 974 cm^{-1}, 1029 cm^{-1}, and 1277 cm^{-1} began to be observed. However, they were not intensified strikingly along with time. These accessory bands were assigned to either surface or bulk-like sulfate species [57]. As SO_2 concentration further increased, the new bands became the most prominent bands on the whole spectrum, demonstrating that S species conquered N species and took up the active sites. Fortunately, the bands at 1382 cm^{-1} and 1473 cm^{-1} were still reserved to launch NO oxidation.

The in-situ DRIFTS measurements under the same conditions were conducted over MnCeFe catalyst, shown in Figure 9. NO-O_2 co-adsorption resulted in N species accumulation on catalyst surface, corresponding to these bands at 1270 cm^{-1}, 1310 cm^{-1}, 1360 cm^{-1}, and 1466 cm^{-1} observed in Figure 9a. Interestingly, compared with MnCe in Figure 8a, the new band at 1270 cm^{-1} (the bidentate nitrate), did not disappear under SO_2 impact in Figure 9b, and even intensified along with time. Also, no shift on the band position was detected. Meanwhile, the other bands at 1360 cm^{-1} and 1466 cm^{-1} shifted to a little higher wave-number, but maintained its intensity. It can be speculated that the positive SO_2 resistance performance of MnCeFe could be related to these undestroyed N species on catalyst surface. Not surprisingly, the bands linked to S species were also intensified. Unlike MnCe,

the band at 1118 cm^{-1} was not the dominated one anymore. Other bands at 1029 cm^{-1} and 1230 cm^{-1} also occupied almost equal status.

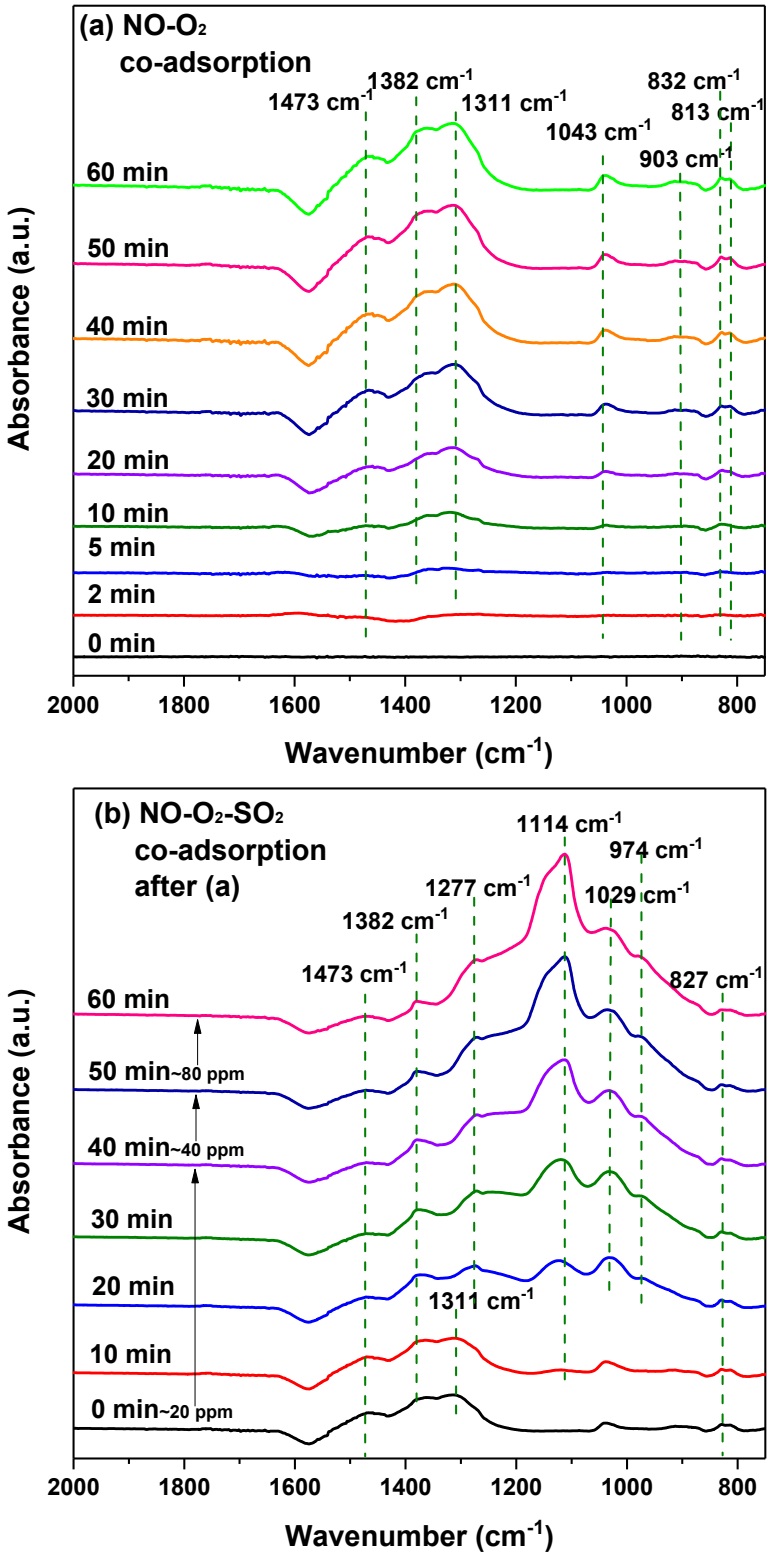

Figure 8. In-situ DRIFTS spectra of MnCe during NO–O_2 co-adsorption ((**a**) 200 ppm NO–10% O_2, N_2 balance and (**b**) 20~40~80 ppm SO_2 addition).

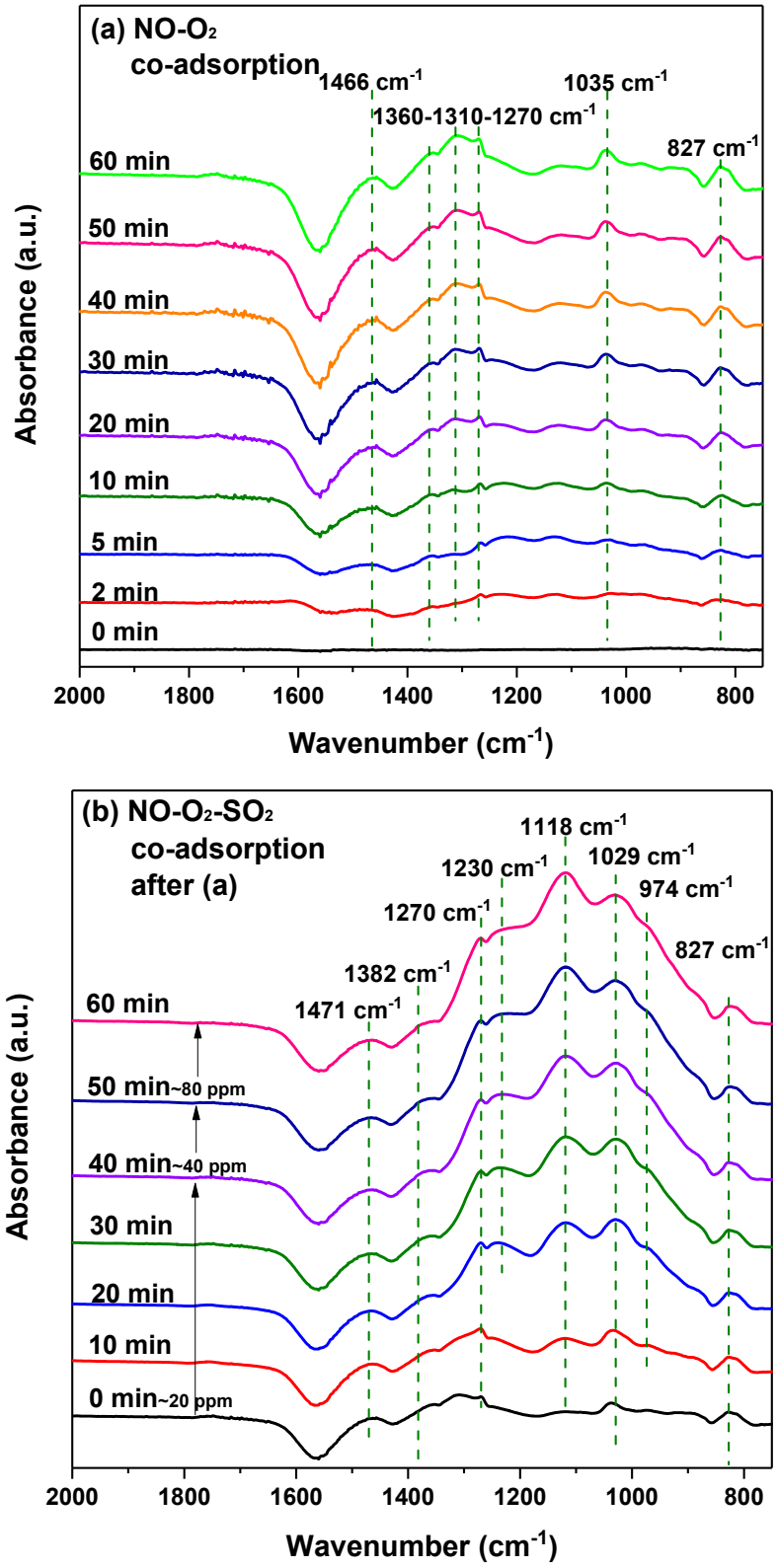

Figure 9. In-situ DRIFTS spectra of MnCeFe during NO–O_2 co-adsorption ((**a**) 200 ppm NO–10% O_2, N_2 balance and (**b**) 20~40~80 ppm SO_2 addition).

3. Experiments and Methods

3.1. Catalyst Preparation

The MnO_x-CeO_2 catalysts were synthesized by the co-precipitation method. A total of 0.01 mol $Ce(NO_3)_3{\cdot}6H_2O$ (AR, 99.0%, Sinopharm, Shanghai, China) and 0.005 mol $Mn(CH_3COO)_2{\cdot}4H_2O$ (AR, 99.9%, Aladdin) were dissolved together in 75 mL distilled water. Subsequently, an excess proportion of $(NH_4)_2CO_3$ (AR, ≥40.0%, Sinopharm, Shanghai, China) solution (120 mL) was instilled into the mixed Ce-Mn precursor solution with a flow rate of 10 mL·min^{-1} under vigorous stirring. After continuously stirring for 2 h, the mixture was aged for another 3 h at room temperature. The precipitate was obtained by centrifugation and washed with deionized water several times. Finally, the product was dried at 110 °C overnight and then calcined in a tube furnace at a target temperature for 3 h with a ramp rate of 1 °C·min^{-1}. Three MnO_x-CeO_2 catalysts were calcined at 350 °C, 450 °C, and 550 °C, respectively, to investigate the calcined temperature effect on catalytic activity. The catalysts were denoted as MnCe(350), MnCe(450), and MnCe(550), respectively. As for the trimetallic catalysts, 0.001 mol $SnCl_4{\cdot}7H_2O$ (AR, 99.0%, Aladdin), $Fe(NO_3)_3{\cdot}9H_2O$ (AR, 98.5%, Sinopharm, Shanghai, China), $Co(NO_3)_2{\cdot}6H_2O$ (AR, 98.5%, Sinopharm, Shanghai, China), $Cr(NO_3)_3{\cdot}9H_2O$ (AR, 99.0%, Sinopharm, Shanghai, China), and $Cu(NO_3)_2{\cdot}3H_2O$ (AR, 99.0%, Sinopharm, Shanghai, China) were separately dissolved together with Mn-Ce precursors above, while the $Mn(CH_3COO)_2{\cdot}4H_2O$ was reduced to 0.004 mol. The rest of the preparation procedure was the same with the former MnCe, and the calcination temperature was fixed at 450 °C. The catalysts were denoted as MnCeSn, MnCeFe, MnCeCo, MnCeCr, and MnCeCu, respectively.

3.2. Activity and Stability Tests

The activity and stability tests of MnO_x-CeO_2 catalysts were conducted in a fixed-bed stainless-steel-tube reactor with an 8 mm internal diameter. A K-type thermocouple was placed in direct contact with the sample to detect the real catalytic temperature. The reaction gas was supplied by cylinder gas (N_2- 99.999%, O_2- 99.999%, NO-5%/balance N_2, SO_2-5%/balance N_2), with the total flow rate of 240 mL·min^{-1}. The initial NO concentration was 200 ppm, and 10% O_2 was injected separately to the reactor as the oxidant. All the samples were sieved to 40~60 mesh and then blended with a moderate amount of quartz sand. A 0.2 g sample was placed in the reactor center with the gas hour space velocity (GHSV) of ~15000 h^{-1}. SO_2 was introduced into the reactor at 250 °C after 100-min stabilization to investigate catalyst resistance to SO_2. NO conversion efficiency was calculated according to the outlet NO and NO_2 concentrations, which were constantly detected by a Fourier transform infrared gas analyzer (Gasmet FTIR DX4000, Vantaa, Finland), as shown in the Equation (1):

$$[\text{Conv.}]_{NO} = [NO_2]_{out}/([NO]_{out} + [NO_2]_{out}) \times 100\ \% \quad (3)$$

where $[\text{Conv.}]_{NO}$ is the NO conversion efficiency, $[NO_2]_{out}$ in ppm is the outlet NO_2 concentration of the reactor, and $[NO]_{out}$ in ppm is the outlet NO concentration of the reactor.

3.3. Catalyst Characterization

The XRD (X-ray diffraction) patterns were detected by using a Rigaku D/MAX-2500 diffractometer (Rigaku Co., Tokyo, Japan). N_2 adsorption-desorption isotherms were measured in a Micromeritics ASAP 2010 analyzer (Micromeritics Instrument Corp, Norcross, GA, USA) at 77 K. The XPS (X-ray photoelectron spectroscopy) was measured through a photoelectron spectrometer (Thermo Scientific Escalab 250Xi, Thermo Fisher Scientific, Waltham, MA, USA) with a standard Al Kα source (1486.6 eV). H_2-TPR measurements were conducted at an automatic temperature programmed chemisorption analyzer (Micromeritics AutoChem II 2920, Micromeritics Instrument Co., Norcross, GA, USA). ~50 mg of catalyst was loaded for TPR tests under the atmosphere 30 mL·min^{-1} 10% H_2/Ar after purged by He (>99.99%) at 120 °C for 1 h. The typical TPR process was started from 100 °C to 800 °C by a ramp of

10 °C·min^{-1}. A Nicolet iS50 FTIR spectrometer (Thermo Nicolet, Madison, WI, USA) equipped with an MCT/A detector was used for in-situ DRIFTS (Diffused Reflectance Infrared Fourier Transform Spectroscopy) experiments. Prior to each test, all samples were pretreated by 80 mL·min^{-1} of N_2 at 120 °C for 1 h. Then, the in-situ spectra were recorded from 600 to 4000 cm^{-1} at 250 °C under specific flue gas. The catalysts after SO_2 poisoning were denoted as MnCe_S and MnCeFe_S, respectively.

4. Conclusions

MnO_x-CeO_2 catalysts were synthesized (molar ratio of Mn/Ce = 0.5) by co-precipitation method to investigate their catalytic activity of NO oxidation. Metal oxides were generated through the thermal decomposition of carbonate composites after the co-precipitation process. Then, the samples were calcined at different temperatures, i.e., 350°C, 450 °C and 550 °C, to evaluate the calcination temperature effect. Subsequently, the third metal (M), i.e., Sn, Fe, Co, Cr, and Cu, was doped separately into MnCe composites to attain trimetallic catalysts with 0.1 M/Ce and 0.4 Mn/Ce molar ratios for NO conversion and SO_2 resistance test. Several conclusions are listed below combined with characterization results.

(1) Higher calcination temperatures brought higher crystallization degree. MnCe catalysts calcined at 350 °C and 450 °C exhibited higher NO conversion than that calcined at 550 °C.
(2) The third metal doping (Sn, Fe, Co and Cr) could reduce crystallization degree, and then improved the surface area or pore volume, but inhibited low temperature reducibility in H_2-TPR, except for MnCeCu.
(3) For SO_2 poisoning, Fe addition into MnCe catalyst could protect Mn and Ce metal oxides from being reduced. In DRIFTS measurement, the decomposition of surface nitrates at SO_2 presence gave evidence to the decreasing NO conversion efficiency. Additionally, the undestroyed parts of nitrate species on the MnCeFe catalyst surface, after SO_2 poisoning, contributed to its better SO_2 tolerance.

Author Contributions: Conceptualization, Z.W. and F.L.; methodology, Z.W.; software, J.S. and Y.L.; validation, Z.W., F.L. and G.C.; investigation, J.S. and H.T.; resources, Y.L.; data curation, J.S. and P.L.; writing—original draft preparation, J.S. and F.L.; writing—review and editing, Z.W., J.S., F.L. and G.C.; funding acquisition, Z.W. All authors read, revised and approved the manuscript.

Funding: This research was funded by the National Key Research and Development Program of China, grant number 2018YFB0605200, and Zhejiang Provincial Natural Science Foundation, grant number LR16E060001.

Acknowledgments: This work was supported by the National Key Research and Development Program of China, grant number 2018YFB0605200, Zhejiang Provincial Natural Science Foundation, grant number LR16E060001, and National Natural Science Foundation of China, grant number 51621005.

Conflicts of Interest: The authors declare no conflict of interest.

References

1. Gao, F.; Tang, X.; Yi, H.; Li, J.; Zhao, S.; Wang, J.; Chu, C.; Li, C. Promotional mechanisms of activity and SO_2 tolerance of Co- or Ni-doped MnO_x-CeO_2 catalysts for SCR of NO_x with NH_3 at low temperature. *Chem. Eng. J.* **2017**, *317*, 20–31. [CrossRef]
2. Adewuyi, Y.G.; Khan, M.A.; Sakyi, N.Y. Kinetics and Modeling of the Removal of Nitric Oxide by Aqueous Sodium Persulfate Simultaneously Activated by Temperature and Fe^{2+}. *Ind. Eng. Chem. Res.* **2014**, *53*, 828–839. [CrossRef]
3. Gao, F.; Tang, X.; Yi, H.; Chu, C.; Li, N.; Li, J.; Zhao, S. In-situ DRIFTS for the mechanistic studies of NO oxidation over α-MnO_2, β-MnO_2 and γ-MnO_2 catalysts. *Chem. Eng. J.* **2017**, *322*, 525–537. [CrossRef]
4. Chen, H.; Wang, Y.; Lyu, Y.-K. High catalytic activity of Mn-based catalyst in NO oxidation at low temperature and over a wide temperature span. *Mol. Catal.* **2018**, *454*, 21–29. [CrossRef]
5. Hong, Z.; Wang, Z.; Li, X. Catalytic oxidation of nitric oxide (NO) over different catalysts: An overview. *Catal. Sci. Technol.* **2017**, *7*, 3440–3452. [CrossRef]

6. Hao, R.; Zhang, Y.; Wang, Z.; Li, Y.; Yuan, B.; Mao, X.; Zhao, Y. An advanced wet method for simultaneous removal of SO_2 and NO from coal-fired flue gas by utilizing a complex absorbent. *Chem. Eng. J.* **2017**, *307*, 562–571. [CrossRef]
7. Liu, Y.; Wang, Q.; Pan, J. Novel Process of Simultaneous Removal of Nitric Oxide and Sulfur Dioxide Using a Vacuum Ultraviolet (VUV)-Activated $O_2/H_2O/H_2O_2$ System in A Wet VUV-Spraying Reactor. *Environ. Sci. Technol.* **2016**, *50*, 12966–12975. [CrossRef] [PubMed]
8. Park, H.W.; Choi, S.; Park, D.W. Simultaneous treatment of NO and SO_2 with aqueous $NaClO_2$ solution in a wet scrubber combined with a plasma electrostatic precipitator. *J. Hazard. Mater.* **2015**, *285*, 117–126. [CrossRef] [PubMed]
9. Zhang, Y.; You, R.; Liu, D.; Liu, C.; Li, X.; Tian, Y.; Jiang, Z.; Zhang, S.; Huang, Y.; Zha, Y. Carbonates-based noble metal-free lean NO_x trap catalysts MO_x–$K_2CO_3/K_2Ti_8O_{17}$ (M= Ce, Fe, Cu, Co) with superior catalytic performance. *Appl. Surf. Sci.* **2015**, *357*, 2260–2276. [CrossRef]
10. Zhang, S.; Li, H.; Zhong, Q. Promotional effect of F-doped V_2O_5–WO_3/TiO_2 catalyst for NH_3-SCR of NO at low-temperature. *Appl. Catal. A Gen.* **2012**, *435*, 156–162. [CrossRef]
11. Scholz, C.; Gangwal, V.; de Croon, M.; Schouten, J. Influence of CO_2 and H_2O on NOx storage and reduction on a Pt–Ba/γ-Al_2O_3 catalyst. *Appl. Catal. B Environ.* **2007**, *71*, 143–150. [CrossRef]
12. Ma, J.; Wang, C.; He, H. Transition metal doped cryptomelane-type manganese oxide catalysts for ozone decomposition. *Appl. Catal. B Environ.* **2017**, *201*, 503–510. [CrossRef]
13. Guo, Z.; Liang, Q.-H.; Yang, Z.; Liu, S.; Huang, Z.-H.; Kang, F. Modifying porous carbon nanofibers with MnO_x–CeO_2–Al_2O_3 mixed oxides for NO catalytic oxidation at room temperature. *Catal. Sci. Technol.* **2016**, *6*, 422–425. [CrossRef]
14. Wang, X.; Wu, G.; Wang, F.; Liu, H.; Jin, T. Solvent-free selective oxidation of toluene with O_2 catalysed by anion modified mesoporous mixed oxides with high thermal stability. *Catal. Commun.* **2017**, *98*, 107–111. [CrossRef]
15. Guo, Y.; Wei, H.; Zhao, G.; Ma, X.; Zhu, W.; Yang, Y. Low temperature catalytic performance of coal-fired flue gas oxidation over Mn-Co-Ce-O_x. *Fuel* **2017**, *206*, 318–324. [CrossRef]
16. Wang, W.; Guo, R.; Pan, W.; Hu, G. Low temperature catalytic oxidation of NO over different-shaped CeO_2. *J. Rare Earths* **2018**, *36*, 588–593. [CrossRef]
17. Wang, A.; Guo, Y.; Gao, F.; Peden, C.H.F. Ambient-temperature NO oxidation over amorphous CrO_x-ZrO_2 mixed oxide catalysts: Significant promoting effect of ZrO_2. *Appl. Catal. B Environ.* **2017**, *202*, 706–714. [CrossRef]
18. Mingshan, C.; Yuan, L.; Xinquan, W.; Jun, W.; Meiqing, S. Effect of preparation method on MnO_x-CeO_2 catalysts for NO oxidation. *J. Rare Earths* **2013**, *31*, 572–576.
19. Qi, G.; Li, W. NO oxidation to NO_2 over manganese-cerium mixed oxides. *Catal. Today* **2015**, *258*, 205–213. [CrossRef]
20. Liang, Q.; Wu, X.; Weng, D.; Xu, H. Oxygen activation on Cu/Mn–Ce mixed oxides and the role in diesel soot oxidation. *Catal. Today* **2008**, *139*, 113–118. [CrossRef]
21. Zhang, H.; Zhou, C.; Galvez, M.E.; Da Costa, P.; Chen, Y. MnO_x-CeO_2 mixed oxides as the catalyst for NO-assisted soot oxidation: The key role of NO adsorption/desorption on catalytic activity. *Appl. Surf. Sci.* **2018**, *462*, 678–684. [CrossRef]
22. Wang, P.; Su, S.; Xiang, J.; You, H.; Cao, F.; Sun, L.; Hu, S.; Zhang, Y. Catalytic oxidation of Hg^0 by MnO_x–CeO_2/γ-Al_2O_3 catalyst at low temperatures. *Chemosphere* **2014**, *101*, 49–54. [CrossRef] [PubMed]
23. Xie, Y.; Li, C.; Zhao, L.; Zhang, J.; Zeng, G.; Zhang, X.; Zhang, W.; Tao, S. Experimental study on Hg^0 removal from flue gas over columnar MnO_x-CeO_2/activated coke. *Appl. Surf. Sci.* **2015**, *333*, 59–67. [CrossRef]
24. Cuo, Z.; Deng, Y.; Li, W.; Peng, S.; Zhao, F.; Liu, H.; Chen, Y. Monolithic Mn/Ce-based catalyst of fibrous ceramic membrane for complete oxidation of benzene. *Appl. Surf. Sci.* **2018**, *456*, 594–601. [CrossRef]
25. Wang, Y.; Deng, W.; Wang, Y.; Guo, L.; Ishihara, T. A comparative study of the catalytic oxidation of chlorobenzene and toluene over Ce-Mn oxides. *Mol. Catal.* **2018**, *459*, 61–70. [CrossRef]
26. Wang, Z.; Lin, F.; Jiang, S.; Qiu, K.; Kuang, M.; Whiddon, R.; Cen, K. Ceria substrate–oxide composites as catalyst for highly efficient catalytic oxidation of NO by O_2. *Fuel* **2016**, *166*, 352–360. [CrossRef]
27. Liu, L.; Zheng, C.; Wu, S.; Gao, X.; Ni, M.; Cen, K. Manganese-cerium oxide catalysts prepared by non-thermal plasma for NO oxidation: Effect of O_2 in discharge atmosphere. *Appl. Surf. Sci.* **2017**, *416*, 78–85. [CrossRef]

28. Shen, Q.; Zhang, L.; Sun, N.; Wang, H.; Zhong, L.; He, C.; Wei, W.; Sun, Y. Hollow MnO_x-CeO_2 mixed oxides as highly efficient catalysts in NO oxidation. *Chem. Eng. J.* **2017**, *322*, 46–55. [CrossRef]
29. Wang, Z.; Sun, X.; Liu, J.; Li, X. The NO oxidation performance over $Cu/Ce_{0.8}Zr_{0.2}O_2$ catalyst. *Surf. Interfaces* **2017**, *6*, 103–109. [CrossRef]
30. Lin, F.; He, Y.; Wang, Z.; Ma, Q.; Whiddon, R.; Zhu, Y.; Liu, J. Catalytic oxidation of NO by O_2 over CeO_2–MnO_x: SO_2 poisoning mechanism. *RSC Adv.* **2016**, *6*, 31422–31430. [CrossRef]
31. López, J.M.; Gilbank, A.L.; García, T.; Solsona, B.; Agouram, S.; Torrente-Murciano, L. The prevalence of surface oxygen vacancies over the mobility of bulk oxygen in nanostructured ceria for the total toluene oxidation. *Appl. Catal. B* **2015**, *174–175*, 403–412. [CrossRef]
32. Qi, G.; Yang, R.T.; Chang, R. MnO_x-CeO_2 mixed oxides prepared by co-precipitation for selective catalytic reduction of NO with NH_3 at low temperatures. *Appl. Catal. B* **2004**, *51*, 93–106. [CrossRef]
33. Yang, P.; Yang, S.S.; Shi, Z.N.; Meng, Z.H.; Zhou, R.X. Deep oxidation of chlorinated VOCs over CeO_2-based transition metal mixed oxide catalysts. *Appl. Catal. B* **2015**, *162*, 227–235. [CrossRef]
34. Machida, M.; Uto, M.; Kurogi, D.; Kijima, T. MnO_x-CeO_2 binary oxides for catalytic NO_x sorption at low temperatures. Sorptive removal of NO_x. *Chem. Mater.* **2000**, *12*, 3158–3164. [CrossRef]
35. Ma, C.; Wen, Y.; Yue, Q.; Li, A.; Fu, J.; Zhang, N.; Gai, H.; Zheng, J.; Chen, B.H. Oxygen-vacancy-promoted catalytic wet air oxidation of phenol from MnO_x–CeO_2. *RSC Adv.* **2017**, *7*, 27079–27088. [CrossRef]
36. Wang, T.; Liu, H.; Zhang, X.; Liu, J.; Zhang, Y.; Guo, Y.; Sun, B. Catalytic conversion of NO assisted by plasma over Mn-Ce/ZSM5-multi-walled carbon nanotubes composites: Investigation of acidity, activity and stability of catalyst in the synergic system. *Appl. Surf. Sci.* **2018**, *457*, 187–199. [CrossRef]
37. Tang, X.; Li, Y.; Huang, X.; Xu, Y.; Zhu, H.; Wang, J.; Shen, W. MnO_x–CeO_2 mixed oxide catalysts for complete oxidation of formaldehyde: Effect of preparation method and calcination temperature. *Appl. Catal. B* **2006**, *62*, 265–273. [CrossRef]
38. Zhao, P.; Wang, C.; He, F.; Liu, S. Effect of ceria morphology on the activity of MnO_x/CeO_2 catalysts for the catalytic combustion of chlorobenzene. *RSC Adv.* **2014**, *4*, 45665–45672. [CrossRef]
39. Yan, Q.; Chen, S.; Qiu, L.; Gao, Y.; O'Hare, D.; Wang, Q. The synthesis of $Cu_yMn_zAl_1$-zO_x mixed oxide as a low-temperature NH_3-SCR catalyst with enhanced catalytic performance. *Dalton Trans.* **2018**, *47*, 2992–3004. [CrossRef]
40. Lin, F.; Wang, Z.; Shao, J.; Yuan, D.; He, Y.; Zhu, Y.; Cen, K. Promotional effect of spherical alumina loading with manganese based bimetallic oxides on nitric oxide deep oxidation by ozone. *Chin. J. Catal.* **2017**, *38*, 1270–1280. [CrossRef]
41. Escribano, V.S.; Lopez, E.F.; Gallardo-Amores, J.M.; Martinez, C.D.; Pistarino, C.; Panizza, M.; Resini, C.; Busca, G. A study of a ceria-zirconia-supported manganese oxide catalyst for combustion of diesel soot particles. *Combust. Flame* **2008**, *153*, 97–104. [CrossRef]
42. Lin, F.; Wang, Z.; Ma, Q.; Yang, Y.; Whiddon, R.; Zhu, Y.; Cen, K. Catalytic deep oxidation of NO by ozone over MnO_x loaded spherical alumina catalyst. *Appl. Catal. B Environ.* **2016**, *198*, 100–111. [CrossRef]
43. Yao, X.; Li, L.; Zou, W.; Yu, S.; An, J.; Li, H.; Yang, F.; Dong, L. Preparation, characterization, and catalytic performance of high efficient CeO_2-MnO_x-Al_2O_3 catalysts for NO elimination. *Chin. J. Catal.* **2016**, *37*, 1369–1380. [CrossRef]
44. Hailstone, R.K.; Difrancesco, A.G.; Leong, J.G.; Allston, T.D.; Reed, K.J. A Study of Lattice Expansion in CeO_2 Nanoparticles by Transmission Electron Microscopy. *J. Phys. Chem. C* **2009**, *113*, 15155–15159. [CrossRef]
45. Li, H.; Tang, X.; Yi, H.; Yu, L. Low-temperature catalytic oxidation of NO over Mn-Ce-O_x catalyst. *J. Rare Earths* **2010**, *28*, 64–68. [CrossRef]
46. Cai, W.; Zhao, Y.; Chen, M.; Jiang, X.; Wang, H.; Ou, M.; Wan, S.; Zhong, Q. The formation of 3D spherical Cr-Ce mixed oxides with roughness surface and their enhanced low-temperature NO oxidation. *Chem. Eng. J.* **2018**, *333*, 414–422. [CrossRef]
47. Thampy, S.; Zheng, Y.; Dillon, S.; Liu, C.; Jangjou, Y.; Lee, Y.-J.; Epling, W.S.; Xiong, K.; Chabal, Y.J.; Cho, K.; et al. Superior catalytic performance of Mn-Mullite over Mn-Perovskite for NO oxidation. *Catal. Today* **2018**, *310*, 195–201. [CrossRef]
48. Li, K.; Tang, X.; Yi, H.; Ning, P.; Kang, D.; Wang, C. Low-temperature catalytic oxidation of NO over Mn–Co–Ce–O_x catalyst. *Chem. Eng. J.* **2012**, *192*, 99–104. [CrossRef]
49. Shang, D.; Zhong, Q.; Cai, W. Influence of the preparation method on the catalytic activity of $Co/Zr_{1-x}Ce_xO_2$ for NO oxidation. *J. Mol. Catal. A Chem.* **2015**, *399*, 18–24. [CrossRef]

50. Zhang, L.; Pierce, J.; Leung, V.L.; Wang, D.; Epling, W.S. Characterization of Ceria's Interaction with NO_x and NH_3. *J. Phys. Chem. C* **2013**, *117*, 8282–8289. [CrossRef]
51. Li, Y.; Li, Y.; Wang, P.; Hu, W.; Zhang, S.; Shi, Q.; Zhan, S. Low-temperature selective catalytic reduction of NO_x with NH_3 over $MnFeO_x$ nanorods. *Chem. Eng. J.* **2017**, *330*, 213–222. [CrossRef]
52. Wang, Y.L.; Ge, C.Z.; Zhan, L.; Li, C.; Qiao, W.M.; Ling, L.C. MnO_x-CeO_2/Activated Carbon Honeycomb Catalyst for Selective Catalytic Reduction of NO with NH_3 at Low Temperatures. *Ind. Eng. Chem. Res.* **2012**, *51*, 11667–11673. [CrossRef]
53. Abdulhamid, H.; Fridell, E.; Dawody, J.; Skoglundh, M. In situ FTIR study of SO_2 interaction with $Pt/BaCO_3/Al_2O_3$ NO_x storage catalysts under lean and rich conditions. *J. Catal.* **2006**, *241*, 200–210. [CrossRef]
54. Jin, R.; Liu, Y.; Wang, Y.; Cen, W.; Wu, Z.; Wang, H.; Weng, X. The role of cerium in the improved SO_2 tolerance for NO reduction with NH_3 over Mn-Ce/TiO_2 catalyst at low temperature. *Appl. Catal. B* **2014**, *148–149*, 582–588. [CrossRef]
55. Liu, J.; Guo, R.-T.; Li, M.-Y.; Sun, P.; Liu, S.-M.; Pan, W.-G.; Liu, S.-W.; Sun, X. Enhancement of the SO_2 resistance of Mn/TiO_2 SCR catalyst by Eu modification: A mechanism study. *Fuel* **2018**, *223*, 385–393. [CrossRef]
56. Chang, H.; Chen, X.; Li, J.; Ma, L.; Wang, C.; Liu, C.; Schwank, J.W.; Hao, J. Improvement of activity and SO_2 tolerance of Sn-modified MnO_x-CeO_2 catalysts for NH_3-SCR at low temperatures. *Environ. Sci. Technol.* **2013**, *47*, 5294–5301. [CrossRef]
57. Yamaguchi, T.; Jin, T.; Tanabe, K. Structure of acid sites on sulfur-promoted iron oxide. *J. Phys. Chem.* **1986**, *90*, 3148–3152. [CrossRef]